JGR Space Physics

RESEARCH ARTICLE
10.1029/2025JA034840

Examining Long-Term Changes in the Ionospheric Response to Geomagnetic Activity Over the Past Five Solar Cycles

Maria Gloria Tan Jun Rios[1,2], **Huixin Liu**[2], **and Claudia Borries**[1]

[1]German Aerospace Center, Institute for Solar-Terrestrial Physics, Neustrelitz, Germany, [2]Department of Earth and Planetary Science, Kyushu University, Fukuoka, Japan

Key Points:

- 55 years of *NmF*2 observations from midlatitude stations are used to examine potential long-term trend in ionosphere response to geomagnetic storms
- No clear long-term trend is detected in the response in local summer
- This is likely due to the compensating effects of small CO_2 rise and increasing solar wind forcing during solar cycles 23 and 24

Correspondence to:
M. G. Tan Jun Rios and H. Liu,
maria.tan@dlr.de;
liu.huixin.295@m.kyushu-u.ac.jp

Citation:
Tan Jun Rios, M. G., Liu, H., & Borries, C. (2025). Examining long-term changes in the ionospheric response to geomagnetic activity over the past five solar cycles. *Journal of Geophysical Research: Space Physics*, *130*, e2025JA034840. https://doi.org/10.1029/2025JA034840

Received 4 NOV 2025
Accepted 16 DEC 2025

Abstract

Model simulations indicate that long-term changes in the thermosphere may influence the intensity of the ionospheric response to geomagnetic activity (GA). This study investigates the response of the peak electron density of the ionosphere (*NmF*2) to GA and its consistency across different solar cycles (SCs) to identify any observable long-term variation. Hourly values of *NmF*2 from six ionospheric stations located at midlatitudes in both hemispheres are examined from 1964 to 2019. Residuals of *NmF*2 relative to a background model are analyzed for correlations with various GA indices to assess the ionospheric response to GA. Kp modified (Kpm) exhibits the highest absolute correlation with the *NmF*2 residuals, indicating it as the most suitable index. The observed patterns align with the well-established storm-time characteristics at midlatitudes, showing a predominant negative response during summer morning hours and a positive response during winter afternoons. During summer, there is a marked negative response to GA with sufficiently high correlations for statistical analysis. However, no significant long-term changes in the relationship between *NmF*2 and GA are identified within the Kpm range of 1–5. This is mainly attributed to the combination of small changes in CO_2 concentration (compared to simulation results from models) and increasing solar wind forcing during SC 23 and 24 than previous SCs. During winter, very low correlation between *NmF*2 and GA prohibits the analysis of any long-term changes in their relationship.

1. Introduction

Ionospheric variations over time are a key component of space climate, as they can significantly affect high-frequency radio communications and transionospheric propagation. These variations follow distinct climatological and seasonal patterns (Rishbeth et al., 2000), primarily driven by solar extreme ultraviolet (EUV) radiation. One of the main influences is the quasi 11-year solar cycle (SC), which causes year-to-year changes in ionospheric behavior.

Ionospheric variability has attracted growing interest in the context of global climate change and rising greenhouse gas concentrations. Roble and Dickinson (1989) predicted that a doubling of atmospheric CO_2 would cool the middle and upper atmosphere (300–400 km) by approximately 50 K, which is much more than the surface-level warming. This pronounced cooling occurs because, at higher altitudes where atmospheric density is low, infrared radiation is less frequently reabsorbed, resulting in more efficient radiative energy loss. In parallel with this thermal effect, thermospheric circulation intensifies and atmospheric tides undergo significant modifications (H. Liu et al., 2020). As a result of above thermal and dynamical variations, the upper atmosphere contracts, lowering the altitude of ionization layers, while maximum electron densities may remain relatively unchanged. Observations of declining ionospheric ion temperatures, which are linked to neutral temperatures, also support this cooling effect (Donaldson et al., 2010; Zhang & Holt, 2013). However, long-term trends in the F2 layer exhibit a non-uniform global pattern. For example, the analyses of Upadhyay and Mahajan (1998) based on more than 30 stations around the world found no obvious large-scale spatial structure in *foF2* trends. In contrast, Danilov and Mikhailov (1999) and Mikhailov et al. (2002) argued that *foF2* trends depend on geomagnetic latitude, with stronger trends occurring at high latitudes. More recent studies, such as Cnossen and Franzke (2014), which examined mid-to high-latitude stations, reported predominantly negative trends. Laštovička (2024) mostly agrees with this negative pattern at mid-latitudes, but also emphasizes the strong sensitivity of results to the EUV proxy used to filter solar activity: depending on the proxy chosen, the inferred trends may even reverse sign. It should also be noted that some reported trends may be influenced by secular changes in the geomagnetic field over the period of analysis (Mikhailov & Marin, 2000).

In addition to solar activity, several other factors can significantly influence the electron density of the F2 layer through complex mechanisms. One such factor is the long-term variability in geomagnetic activity (GA), which reflects evolving patterns of magnetospheric forcing in the ionosphere. Another important factor is the long-term change in the Earth's geomagnetic field configuration, including secular variations in the field strength and the geographic distribution of energetic particle precipitation at high latitudes. These changes can significantly alter plasma transport and the spatial structure of ionization (i.e., Cnossen & Richmond, 2008; Cnossen & Richmond, 2013; Elias et al., 2010; Yue et al., 2008). Furthermore, the F2 layer is particularly sensitive to changes in thermospheric dynamics and composition and ionospheric dynamics. In particular, variations in atomic oxygen and molecular nitrogen concentrations affect production and loss processes in the ionosphere (i.e., A. Danilov, 2017; Jakowski et al., 2024). Coupling processes from below, such as planetary waves and tides, also modulate thermospheric composition and ionospheric dynamics, exhibiting spatial and temporal variability (H. Liu et al., 2020).

Most studies on CO_2-induced long-term ionospheric trends focused only on quiet conditions ($\mathrm{Kp} < 3$). Recently, H. Liu et al. (2021), using the Ground-to-topside model of Atmosphere and Ionosphere for Aeronomy, examined how increasing CO_2 in the atmosphere can affect the geomagnetic storm effects on the ionosphere and thermosphere, and how changes in the GA may affect the derivation of CO_2-induced long-term trend in the ionosphere-thermosphere. They found that the CO_2-induced long-term trend in NmF2 is highly variable with latitude and local time (LT). At the same time, increasing CO_2 can significantly enhance the global-averaged ionosphere responses to storms (i.e., more positive response at the topside and more negative response at the bottomside in summer), thus making space weather impacts more severe in the future for both moderate ($\mathrm{Kp} = 3$) and severe storms ($\mathrm{Kp} = 6$). The follow-on study, Pedatella et al. (2025), further examined details of the impact of increasing CO_2 on the ionosphere response to one super geomagnetic storm using simulations from the Whole Atmosphere Community Climate Model—eXtended (WACCM-X). They found the impact varies with latitude, which enhances the responses at auroral and tropical regions, but weakens the response at middle latitudes.

The goal of this research is to investigate if there is an observable long-term effect in the $NmF2$ response to GA. The physical mechanisms that govern ionospheric storms can provide valuable insight into the relationship between ionospheric variations and GA. It is well known that at midlatitudes, positive storms are primarily observed in winter and negative storms during equinox and summer conditions (Prölss, 2013). The nature of the ionospheric disturbance effect is also influenced by the LT of the storm onset. Negative ionospheric storm effects are most frequently observed in the morning, whereas positive storms generally take place in the afternoon and evening (Buonsanto, 1999).

Using H. Liu et al. (2021) and Pedatella et al. (2025) as a theoretical foundation, this study aims to investigate whether long-term changes in the thermosphere have already influenced the magnitude of the $NmF2$ variations associated with GA, based on ionosonde observations. Our analysis focuses on two specific conditions: mid-latitude summer negative response to GA and mid-latitude winter positive response to GA. These are the most prominent ionospheric perturbations related to GA.

Using statistical analyses, this study investigates the central question: *How has the ionospheric $NmF2$ response to GA evolved across SCs since the* 1950s? $NmF2$ data of six midlatitude ionosonde stations in both hemispheres are used for the study. The following approach is used for the investigation:

1. Characterize the $NmF2$ response to GA depending on season and other relevant contextual factors.
2. Identify and select conditions showing a clear and consistent correlation between $NmF2$ and GA, and compute the average magnitude of the associated variations for each SC.
3. Quantify how the $NmF2$ response to GA changes with each SC.
4. Interpret the observed trends in the context of the model results regarding thermospheric cooling and its modulation of the ionospheric response to geomagnetic forcing.

2. Data and Methods

2.1. Ionosonde Data

The peak electron density in the F2 layer, denoted as $NmF2$, is derived from the $foF2$ data using the following relationship (Piggott & Rawer, 1978):

Table 1
Ionosonde Stations Used in This Work, Including the Local Time (LT) Offset (LT (UT+)) Used to Convert UT to LT

Station name	URSI name	LT (UT+)	Geogr. Lat. (°)	Geogr. Long. (°)	Geomag. Lat. (°)	Period of availability
Boulder	BC840	−7	40.00	−105.30	47.72	1958–2024
Port Stanley	PSJ5J	−4	−51.60	−57.90	−42.21	1957–90, 96–2019
Juliusruh	JR055	1	54.60	13.40	53.95	1957–2023
Slough/Chilton	RL052	0	51.50, 51.70	−0.60, −1.33	53.31, 53.41	1957–90, 96–2024
Moscow	MO155	3	55.47	37.30	51.05	1957–95, 2008–2022
Hobart	HO54K	11	−42.90	147.32	−49.77	1950–2024

$$NmF2 = 1.24 \times 10^{10} \cdot (foF2)^2 \tag{1}$$

In this equation, $NmF2$ is expressed in m^{-3} and $foF2$ in MHz.

This study analyzes data from six ionosonde stations located at similar geomagnetic latitudes worldwide, each providing extensive long-term observational records. For the American region, the Boulder and Port Stanley stations are considered. In Europe, the Slough/Chilton station is analyzed, alongside Juliusruh. The Moscow station serves as a representative for the East European region, while the Hobart station is selected for Oceania. Table 1 provides the geographic and geomagnetic coordinates of each ionosonde station used, along with the corresponding periods during which $foF2$ data were available. It is important to note that data obtained from Global Ionospheric Radio Observatory (GIRO) is only considered if it has a confidence score of 70 or higher (refer to Section 5 for details on data availability). Additionally, there is a significant gap in the Moscow data for SC23; however, complete data for SC24 is available. Figure 1 illustrates the location of each ionosonde station on the map, with respect to the geomagnetic equator.

The geomagnetic latitudes in Table 1 were obtained by transforming the geographic coordinates from each ionosonde station using the International Geomagnetic Reference Field (IGRF-14) model for the year 2015. The geomagnetic equator in Figure 1 was obtained in the same way for an altitude of 300 km.

2.2. Geomagnetic Indices

In this study, we employ the geomagnetic indices Kp, Kpm, ap, Hp60, ap60, and am, all derived from mid-latitude magnetometer observations. The Kp index characterizes geomagnetic disturbances on a quasi-logarithmic scale with a temporal resolution of 3 hr (Bartels et al., 1939). The ap index expresses the same variability in linear units of 2 nT and provides a continuous record extending back to 1932 (Mayaud, 1980). The am index, available since

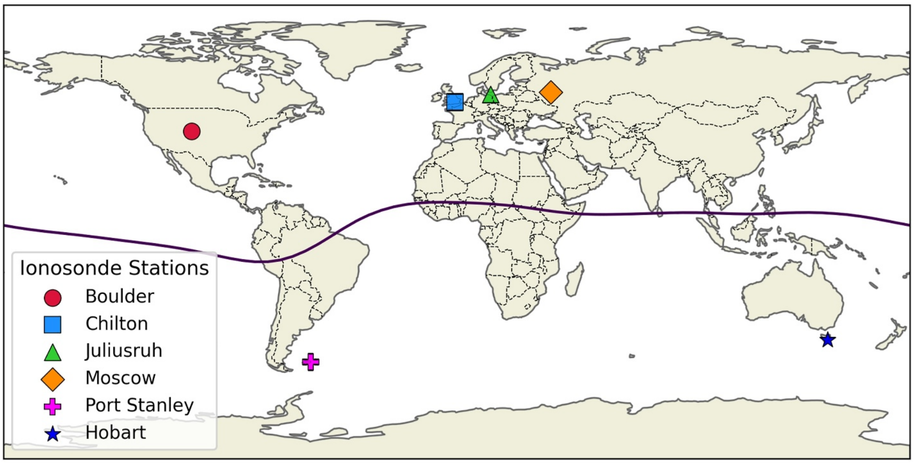

Figure 1. World map with the location of the ionosonde stations used in this work (color markers) and the geomagnetic equator (red line) obtained by using IGRF in 2015.

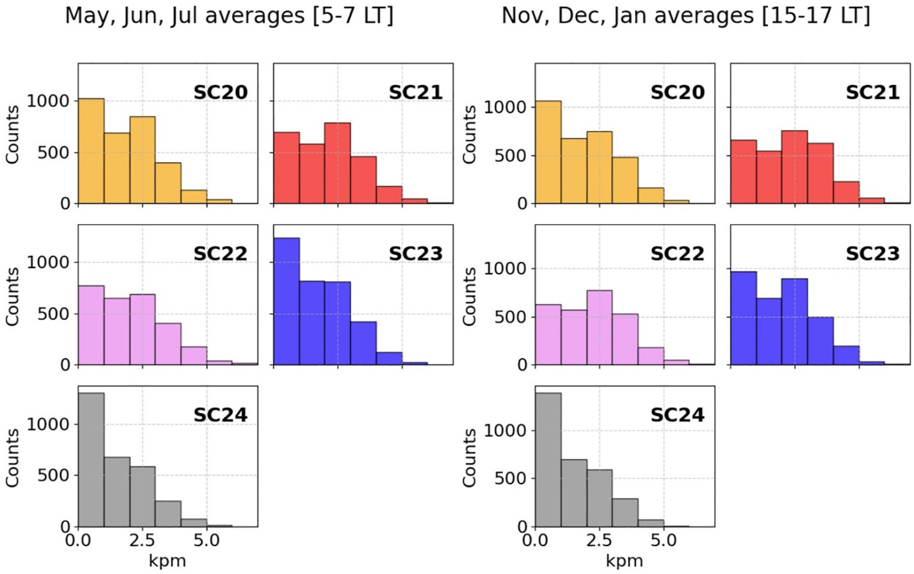

Figure 2. Histograms of data distribution according to Kpm for each solar cycle (from SC20 to SC24) separately. The left panel shows only the data for May, June and July between 5 and 7 local time (LT). The right panel shows the data for November, December and January between 15 to l7 LT.

1959, offers a more global measure by incorporating data from both hemispheres to achieve balanced representation of disturbances. The Kpm index is a variant of Kp in which the quasi-logarithmic steps (0–9, subdivided into thirds) are transformed into continuous values, retaining the 3-hr cadence (Chakraborty & Morley, 2020; Matzka et al., 2021). More recent developments include the Hpo family of indices (Yamazaki et al., 2022), such as Hp60 and ap60, which provide higher temporal resolution (one hour resolution) but are only available since 1995.

In our analysis, we examine the correlations between these indices and $NmF2$. Since $NmF2$ data are hourly, we adapt 3-hr indices by repeating values from the previous observation to match the temporal resolution.

Figure 2 displays the histogram of data distribution for each SC (from SC20 to SC24), categorized by GA levels based on Kpm values. The plots focus specifically on May to July during morning hours and on November to January during afternoon hours, as these selections correspond with subsequent analyses presented later in this study. During the analyzed periods, approximately 98% of the total data falls within the Kpm range of 0–5. This indicates that strong geomagnetic disturbances (Kpm values above 5 or 6) are statistically rare and insufficiently represented to draw robust conclusions. Therefore, we focus on GA up to Kpm = 5 in the following analysis.

2.3. Method

2.3.1. *NmF*2 Residuals

To focus our analysis on the relationship between ionospheric behavior and GA, we aim to remove the contributions from solar activity in our data. We utilize the modeling method described in Tan Jun Rios et al. (2025), where the ionospheric response to solar flux is expressed through cubic fitting for each month of every SC for each LT. This model is generated using data only from periods of low GA. For more details on the solar activity filtering model, please refer to Sections 2.3 and 2.4 of Tan Jun Rios et al. (2025).

$$\Delta NmF2 = NmF2_{\mathrm{obs}} - NmF2_{\mathrm{model}} \tag{2}$$

$$\Delta \mathrm{NmF2}_{\mathrm{perc}} = \frac{\Delta \mathrm{NmF2}}{\mathrm{NmF2}_{\mathrm{model}}} \times 100\% \tag{3}$$

The differences between the observed (measured) $NmF2$ data from the ionosonde ($NmF2_{\mathrm{obs}}$), and the predicted $NmF2$ values generated by cubic regressions ($NmF2_{\mathrm{model}}$) are referred to as residuals (ΔNmF2, c.f. Equation 2). The ΔNmF2 represents the variations in $NmF2$ that cannot be explained by solar activity. These variations are

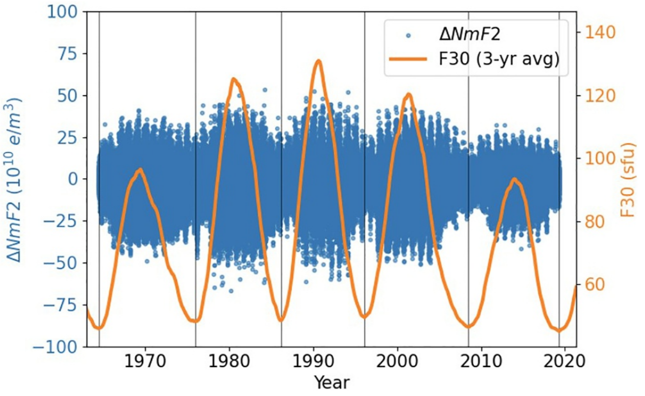

Figure 3. ΔNmF2 data from Juliusruh (scatter plot) and the 3-year moving average of F30 (orange line). Vertical black lines indicate definition of the solar cycles (from SC20 to SC24).

assumed to capture the relationship between *NmF*2 and GA, impact of plasmaspheric fluxes, atmospheric influences from below and errors in observation. These values show a clear SC dependence as shown in Figure 3 where the ΔNmF2 and the 3-year moving average of F30 are plotted. To reduce the SC dependence, the relative or percentage difference to $NmF2_{\text{model}}$ is computed ($\Delta\text{NmF2}_{\text{perc}}$) using Equation 3. The advantages of using relative values instead of absolute ones are discussed and used in many previous works. (i.e., Bremer, 1998; Upadhyay & Mahajan, 1998; Danilov & Mikhailov, 1999; Mikhailov & Marin, 2000).

2.3.2. Correlation Between ΔNmF2 With GA Indices

Understanding the correlation between GA and *NmF*2 variations requires considering seasonal, LT, and time delay dependencies, as these factors significantly modulate the ionospheric response. The sensitivity of *NmF*2 to geomagnetic disturbances varies with season due to changes in thermospheric composition, solar exposure, and background ionospheric conditions (Mendillo et al., 2002; Zou et al., 2014). Local time dependence is critical, as the ionosphere's daytime and nighttime behaviors are governed by different physical processes (Buonsanto, 1999; Lei et al., 2008). Additionally, the ionospheric time delay to geomagnetic storms can range from minutes to several hours, depending on latitude, storm magnitude, and dominant coupling mechanisms such as Prompt Penetration Electric Fields (PPEF) and disturbance dynamo effects (Fuller-Rowell et al., 1994; Tsurutani et al., 2004). Here, the different method used to account for these factors are presented.

The Pearson correlation coefficient defined in Equation 4 is used as a quantitative measure of the linear relationship between ΔNmF2 and the GA indices, thus, as an indicator of their correlation.

$$r_{xy} = \frac{\sum_{i=1}^{n}(x_i - \bar{x})\left(y_i - \bar{y}\right)}{\sqrt{\sum_{i=1}^{n}(x_i - \bar{x})^2}\sqrt{\sum_{i=1}^{n}\left(y_i - \bar{y}\right)^2}}, \tag{4}$$

where x_i and y_i are the paired values of the two variables, in this case ΔNmF2 or $\Delta\text{NmF2}_{\text{perc}}$ and the GA index, $\bar{x}$ and $\bar{y}$ are their respective means, and n is the number of observations. The coefficient r_{xy} ranges from -1 to $+1$. Values close to $+(-)1$ indicate strong positive (negative) linear correlation and values near 0 suggest no linear relationship.

To quantify the uncertainty of the estimated correlation, confidence intervals are calculated using Fisher's z-transformation. This transformation converts the correlation coefficient r into a variable z with an approximately normal distribution, enabling the computation of confidence bounds. The transformation is given by:

$$z = \tanh^{-1}(r) = \frac{1}{2}\ln\left(\frac{1+r}{1-r}\right) \tag{5}$$

The standard error of z is approximated by:

$$\text{SE} = \frac{1}{\sqrt{n-3}} \tag{6}$$

where n is the sample size. A confidence interval for z is then computed using the critical values of the normal distribution. Finally, the bounds are transformed back to the correlation scale via the inverse Fisher transformation:

$$r = \tanh(z) = \frac{e^{2z}-1}{e^{2z}+1} \tag{7}$$

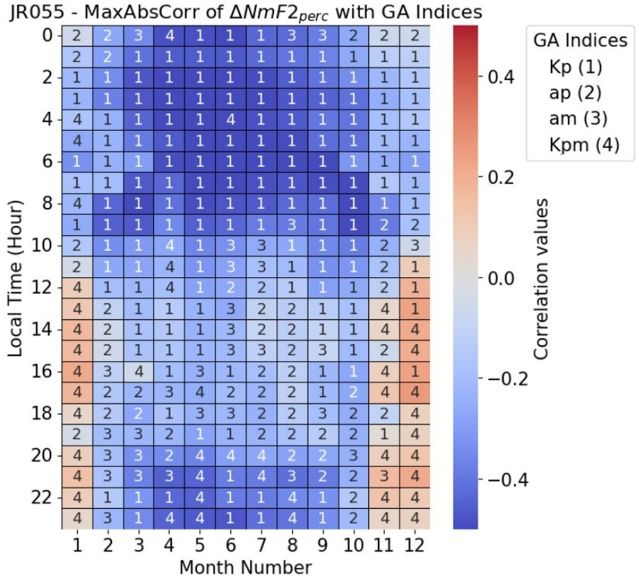

Local Time (Hour)	1	2	3	4	5	6	7	8	9	10	11	12
0	2	2	3	4	1	1	1	3	3	2	2	2
	2	2	1	1	1	1	1	1	1	1	1	1
2	1	1	1	1	1	1	1	1	1	1	1	1
	1	1	1	1	1	1	1	1	1	1	1	1
4	4	1	1	1	1	4	1	1	1	1	1	1
	4	1	1	1	1	1	1	1	1	1	1	1
6	1	1	1	1	1	1	1	1	1	1	1	1
	1	1	1	1	1	1	1	1	1	1	1	1
8	4	1	1	1	1	1	1	1	1	1	1	1
	1	1	1	1	1	1	1	3	1	1	2	2
10	2	1	1	4	1	3	3	1	1	1	2	3
	2	1	1	4	1	3	3	1	1	1	2	1
12	4	1	1	4	1	2	2	1	1	1	2	1
	4	2	1	1	1	3	2	2	1	1	4	1
14	4	2	1	1	1	3	2	2	1	1	4	4
	4	2	1	1	1	3	3	2	3	1	2	4
16	4	3	4	1	3	1	2	2	1	1	4	1
	4	2	2	3	4	2	2	2	1	2	4	4
18	4	2	2	1	3	3	2	2	3	2	2	4
	2	3	3	2	1	1	2	2	2	2	1	4
20	4	3	3	2	4	4	4	2	2	3	4	4
	4	3	3	3	4	1	4	3	2	2	3	4
22	4	1	1	1	4	1	1	4	1	2	4	4
	4	3	1	4	4	1	1	4	1	2	4	4

Figure 4. Heat-map of maximum absolute correlation values between ΔNmF2$_{perc}$ from Juliusruh and different geomagnetic activities indices [(1)Kp; (2)ap; (3)am; (5)Kpm] for local time hour and month.

This approach provides a statistically robust interval estimate for the true population correlation coefficient (Bonett & Wright, 2000). The correlation value is considered insignificant in this work if the confidence interval includes zero. Importantly, this criterion is mathematically equivalent to testing whether the p-value of the correlation is greater than the significance threshold (e.g., 0.05). Both approaches assess whether the observed correlation could plausibly arise under the null hypothesis of no true association, and therefore lead to the same conclusion regarding statistical significance.

Heatmaps are frequently used in this work to assign different colors to each correlation coefficient, illustrating the variation in correlation between two conditions, for example, LT and months. Figure 4 presents a heatmap illustrating the correlation between ΔNmF2$_{perc}$ and various GA indices, using Juliusruh data from SC20 to SC24, spanning from 1964 to 2019, during which the data is available for each complete SC. The vertical axis represents LT hours, while the horizontal axis corresponds to the calendar months.

Each GA index shows distinct sensitivity patterns, but the overall structure of the correlation maps remains consistent across all indices. The color scale indicates correlation values, ranging from −0.5 to 0.5. This heatmap compares the correlation values obtained from the different GA indices and identifies the maximum absolute correlation value. Within each grid square, the GA index with the strongest correlation is indicated by a number: (a) Kp, (b) ap, (c) am, and (d) Kpm, with the corresponding color representing the correlation value.

The Hp60 index, available from 1985 onward, was also evaluated; however, it did not produce stronger correlations than Kp or Kpm, and its limited temporal coverage leads to its exclusion from the analysis.

Overall, the correlations are generally modest, with absolute values rarely exceeding 0.3 and a predominance of negative values. Notably, during December, January, and February, there is a discernible shift toward positive correlations, particularly around noon and afternoon LT hours, as indicated by red hues.

The highest absolute correlations, reaching up to −0.5, occur in the morning hours of May, June, and July. Hence, these summer months provide the strongest signals, making them particularly suitable for studying long-term variations. In contrast, the correlations in the remaining months are typically weaker.

As shown in Figure 4, the correlation between ΔNmF2$_{perc}$ and various GA indices is predominantly negative for all months and local times, except for noon and afternoon during the local winter months, when the correlation becomes positive. This agrees with the well-known pattern of ionospheric storm responses in midlatitudes (i.e., Field & Rishbeth, 1997). These seasonal and local-time–dependent correlation features are consistent with the mechanisms known to produce positive and negative ionospheric storm effects (i.e., Prölss, 1995; Fuller-Rowell et al., 1996; Mendillo, 2006; A. Danilov, 2013). During winter, enhanced ionization (positive storm effects) in mid-latitudes typically arise within a few hours after the storm onset from either equatorward thermospheric winds or prompt penetration electric fields or both. Also, the equatorward expansion of the polar ionization enhancements can cause increased electron density. These effects can also occur during summer, but since the background thermospheric winds are equatorward (opposite to winter condition), the strength and timing of positive storms is different in summer. In fact, the electron density depletion (negative storm) is the more prominent storm characteristic in summer. It occurs after several hours and is typically the result of composition changes and the Disturbance Dynamo Electric Field (DDEF), which need some hours to build up (i.e., Blanc & Richmond, 1980; Prölss, 1995, 2013; Fejer et al., 2016). Thus, the observed correlation behavior reflects the same physical processes discussed in previous works on midlatitude ionospheric storm responses.

Under disturbed conditions, the summer hemisphere experienced a daily-averaged depletion in $NmF2$, while the winter hemisphere exhibited an increase, with equinox resembling summer behavior. This seasonal pattern may also reflect differences in lower-atmosphere forcing. Planetary waves, tides, and gravity waves are known to propagate upward and modulate $NmF2$, adding variability (Borries et al., 2007). Since the efficiency of upward

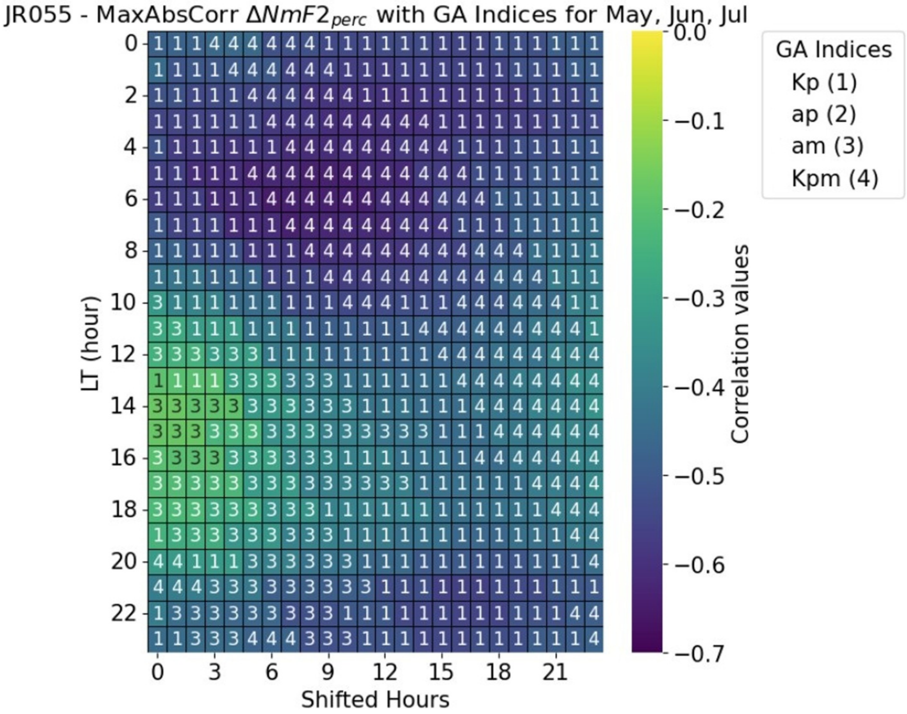

Figure 5. Heat-map for the months of May, June and July with maximum absolute correlation values between $\Delta NmF2_{perc}$ from Juliusruh and different geomagnetic activities indices [(1)Kp; (2)ap; (3)am; (5)Kpm] for each local time hour and the shifted (delay) hour.

wave propagation is strongly seasonal, with summer conditions tending to filter a larger portion of these waves (Malhotra et al., 2025), the background atmospheric noise is generally lower in summer. This reduced variability may contribute to the clearer $\Delta NmF2_{perc}$ response to GA during that season.

2.3.3. Identification of Conditions With the Clearest ΔNmF2 Response to GA

In this section, we further examine the correlation of ΔNmF2 and GA for summer conditions during morning hours, where the relationship is strongly negative and winter afternoon conditions, where the relationship is positive. In both cases, a fundamental first step is the identification of optimal conditions for analyzing the ΔNmF2–GA relationship. To achieve this, we utilize the Pearson correlation coefficient, time delays, and moving windows. Since changes in the magnetosphere are not immediately reflected in the ionosphere, applying a time shift between the GA indices and $NmF2$ can improve the observed correlation. This approach allows for the inclusion of delayed effects due to energy transfer processes and propagation delays in the thermosphere-ionosphere system, improving the accuracy of statistical relationships (Mikhailov et al., 2002). In this work, various time shifts are tested to identify the temporal offset that yields the highest correlation between ΔNmF2 and GA indices. As an example for Juliusruh data, Figure 5 displays a correlation heat map derived from data collected during the three summer months: May, June, and July. The vertical axis represents LT hours, while the horizontal axis indicates time delays (ranging from 0 to 23 hr) applied to the GA indices. Similar to Figure 4, this figure compares various GA indices, focusing only on those that produce the highest absolute correlation values. The color bar illustrates correlation values that range from −0.7 to 0.0, emphasizing a negative correlation.

From this figure, we observe that the maximum absolute correlation value is found at 6 LT. Here, the percentage of $\Delta NmF2_{perc}$ shows a correlation with the Kpm index under a time-shift condition of approximately 7–10 hr, resulting in a correlation value of around −0.6.

Several studies have shown that incorporating a moving average or smoothing window over the GA indices can further increase their correlation with ionospheric parameters by reducing short-term fluctuations and emphasizing the more persistent components of geomagnetic forcing (Astafyeva et al., 2015; Blanch et al., 2012). For

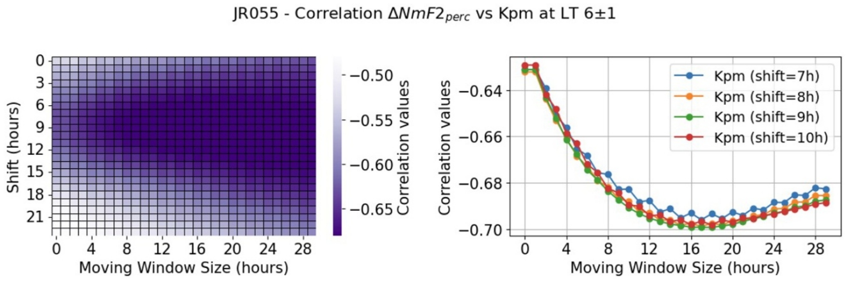

Figure 6. Left Panel: Heat map with correlation values for Juliusruh in May, June and July at 5–7 local time between $\Delta NmF2_{perc}$ and Kpm for diferent shift hours and moving average window size in hours. Right Panel: The correlation values with shifts between 7 and 10 hr for different moving window sizes.

that reason, multiple smoothing window sizes are tested to identify the optimal configuration that maximizes the correlation with *NmF*2 while preserving meaningful geophysical variability.

Continuing with the example of the summer morning conditions in Juliusruh, we aim to enhance the correlation values shown in Figure 5 by increasing the absolute correlation. To achieve this, the geomagnetic index is smoothed using different moving window sizes. The left panel of Figure 6 illustrates the correlation values between $\Delta NmF2_{perc}$ and Kpm at 5–7 LT, with the vertical axis showing the shifted hours and the horizontal axis indicating the moving window size in hours used to smooth Kpm. Notably, there are many combinations of shifted hours and window sizes that yield very similar correlation values. Therefore, the right panel of Figure 6 presents the correlation values between $\Delta NmF2_{perc}$ and Kpm at 5–7 LT, highlighting different shifts of 7–10 hr across various moving window sizes in order to see more detailed the variation in the correlation under this conditions. Although the correlation for the different shift times are quite close, the correlation using a shift of 9 hr is the lowest. Additionally, a moving window size between 13 and 20 hr results in an increase of approximately 0.06 in absolute correlation. For convenience, we will use just one window size for averaging, so we chose a window size of 17 hr.

In summary, our analysis indicates that the maximum absolute correlation between $\Delta NmF2_{perc}$ and Kpm in Juliusruh during May, June, and July is observed at 6 LT, corresponding to a 9-hr time shift and a 17-hr moving average window. These conditions, which most clearly capture the ionospheric *NmF*2 response to GA, are employed to investigate the temporal variability of this relation.

2.3.4. ΔNmF2 Response to GA During Different SCs

The method outlined in Tan Jun Rios et al. (2025) is utilized to analyze the temporal variation of the relationship between *NmF*2 and GA. Data is organized by SC to evaluate the ionospheric response within each cycle individually, allowing for comparisons across different SCs to identify long-term variations over time. The periods corresponding to the most recent SCs are presented in Table 1 and Figure 1 in Tan Jun Rios et al. (2025). This study analyses the changes in the relationship between $\Delta NmF2_{perc}$ and the geomagnetic index across various SCs, to compare relations observed in these different cycles.

After establishing the optimal conditions for analyzing the relationship between ionospheric variations and GA, as described in the preceding section, we examine how this relationship changes over time, comparing the results for each SC.

Using the conditions that exhibited the clearest relationship between *NmF*2 and GA during the summer months, as discussed previously, Figure 7 presents scatter plots of $\Delta NmF2_{perc}$ versus Kpm. The data is categorized according to their respective SCs, with SC21 shown here as a representative example. Data point in gray corresponds specifically to May, June, and July of SC21 at 6 LT. Given the clear linear distribution of the data, we perform a linear fit and apply an outlier removal procedure based on the residuals. Specifically, data points that lie beyond two standard deviations from the fitted line are excluded for each SC. This process removes only a small fraction of the data, approximately 0.5%–2.5% per each group, depending on the cycle, and helps eliminating anomalous values that deviate from the general pattern. In the example of SC21, the data removed represent 2.3% of the total data in the plot.

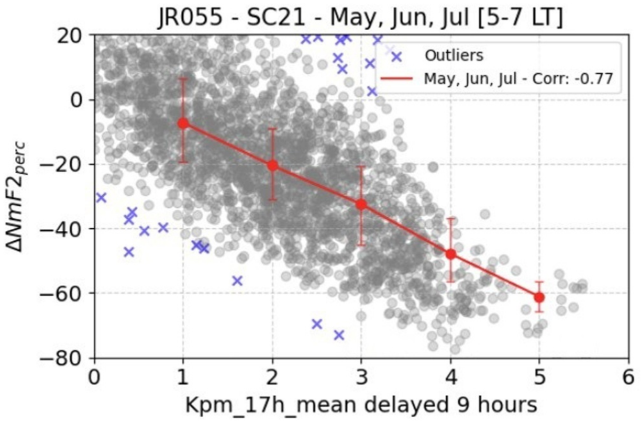

Figure 7. ΔNmF2$_{perc}$ for Juliusruh in May, June and July at 5, 6, 7 local time versus Kpm in SC21, utilizing a 9-hr shift and a 17-hr moving window (gray dots) and median values for each window size of 2 Kpm with steps of 1 Kpm with their corresponding lower and upper quartiles (red dots with error bars). Outliers (blue crosses) are indicated in the plot but do not considered for calculations.

To facilitate comparisons between SCs, we use a binning-based plotting method to display the median ionospheric response to levels of GA. Similar to the approach used by Chen et al. (2022). For each SC separately, the ΔNmF2$_{perc}$ data has been organized into moving bins of size 2 Kpm, with a 1 Kpm step, to better illustrate the variations of ΔNmF2$_{perc}$ in response to each GA level. For instance, the first window covers Kpm values from 0 to 2, the second window ranges from 1 to 3, and so on. For each bin, the median of the residual values is calculated to provide a robust central estimate, as it is less sensitive to extreme outliers than the mean. However, results using mean values show only minor differences, confirming the stability of the trend regardless of the chosen measure of central tendency. The interquartile range, defined as the difference between the upper (75th percentile) and lower (25th percentile) quartiles, is used to represent the spread of the data. The lower and upper quartiles are plotted as error bars to convey the statistical variability around the median. Bins with fewer than 10 data points are explicitly flagged to indicate their limited statistical reliability and should be interpreted with caution. It is important to emphasize that this analysis relies solely on descriptive statistical techniques, and no curve fitting or regression modeling is applied to the binned data.

In Figure 7, the red dots represent the median values of the binned data and are positioned at the center of each bin size. The accompanying red error bars indicate the corresponding lower and upper quartiles. Medians based on fewer than 10 values are marked with crosses. The outliers are indicated with blue crosses in the plot but they are not considered for the rest of the analysis.

Figure 8 presents the relationship between $NmF2$ and GA for each SC separately. Again, the median values of the binned ΔNmF2$_{perc}$ data are in the center of each bin, along with error bars that correspond to the lower and upper quartiles. This figure mirrors the format of Figure 7, but now includes all SCs separately, making it easier to observe variations in response during each SC. The differences among various SCs are not easily recognizable; in fact, all SCs exhibit a similar response to GA and overlap with one another except for SC24 at Kpm = 5, as illustrated in Figure 8. In the following sections, we will apply this analysis method to analyze all six stations.

3. Results

3.1. Negative Correlation Between ΔNmF2 and GA During Summer Mornings

Figure 9 presents a correlation heat map between ΔNmF2$_{perc}$ and Kpm for specific local times and delayed hours at each selected station on the local summer months: May, June, and July in the Northern Hemisphere, and November, December, and January in the Southern Hemisphere. This plot is similar to the one in Figure 5 for Juliusruh, but it only considers Kpm for the correlations across each ionosonde station. White contour lines enclose regions with not statistically significant correlations.

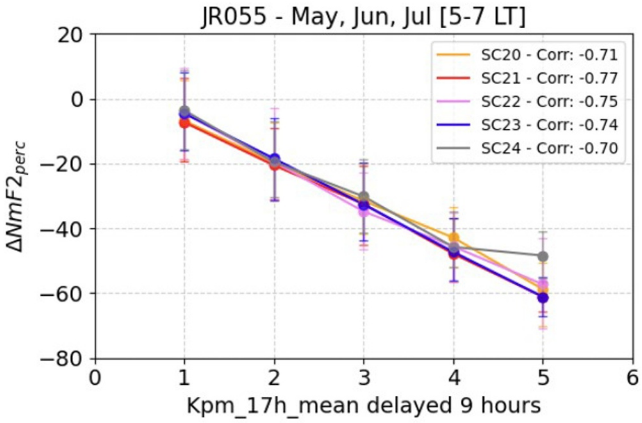

Figure 8. Median values for ΔNmF2$_{perc}$ Juliusruh data for May, June, and July between 5 and 7 local time in a 2 Kpm moving window with steps of 1 Kpm for each solar cycle separately. The error bars represent their corresponding lower and upper quartiles.

All correlation heat maps display a similar pattern, showing high absolute correlation values during the morning hours (between 4 and 8 LT) when using delays of 7–9 hr. The patterns for Moscow (MO155) and Chilton (RL052) are particularly similar to those for Juliusruh (JR055), with lower correlation values observed during noon and the afternoon, followed by an increase at night. Boulder (BC840) and Port Stanley (PSJ5J) exhibit lower correlation values, indicated by the increased presence of green and yellow colors compared to the other stations. This is consistent with Field and Rishbeth (1997), who found that the magnitude of $NmF2$ depletion was greater at higher magnetic latitudes. Additionally, Chen et al. (2022) found that the negative ionospheric correlation with GA at midlatitudes varied seasonally,

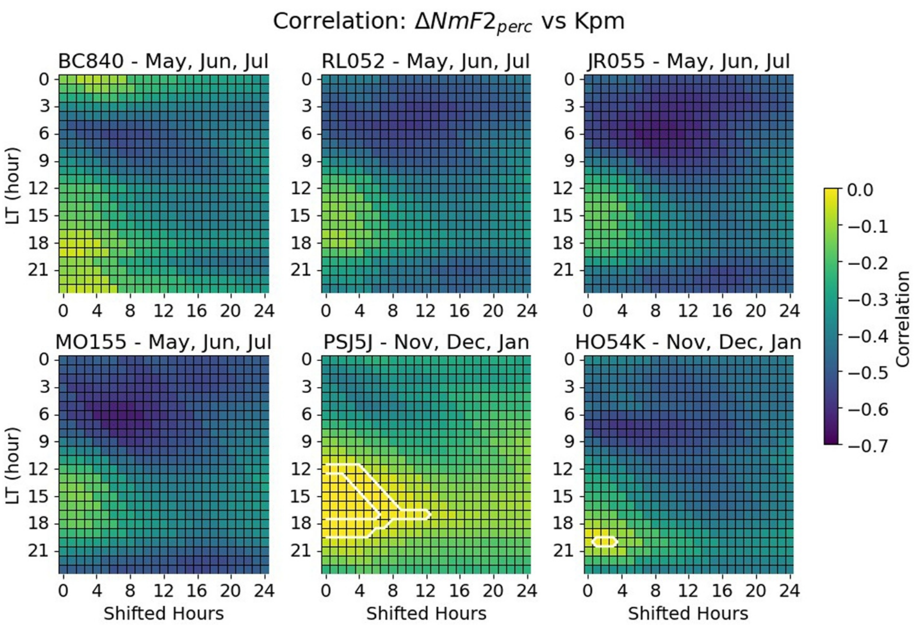

Figure 9. Heat maps showing the maximum absolute correlation values between $\Delta NmF2_{perc}$ and Kpm index for each local time hour, including a shifted (delayed) hour during summer. Analysis includes Northern Hemisphere ionosonde stations (Boulder: BC840; Slough/Chilton: RL052; Juliusruh: JR055; Moscow: MO155) during May, June, and July, and Southern Hemisphere stations (Port Stanley: PSJ5J; Hobart: HO54K) during November, December, and January. White lines encapsulate insignificant correlations.

being stronger in summer and equinox periods and weaker during local winter. While their results are consistent with our findings regarding seasonal behavior, the correlation values reported by Chen et al. (2022). Are generally lower. This difference is likely due to their analysis being limited to local noon conditions.

The procedure used in Juliusruh to identify the conditions that yield the clearest relationship between *NmF*2 and GA, as explained in Section 2.3.3, is also applied to all selected midlatitude stations. Correlation heat maps are generated to determine which GA index shows the highest correlations, and the optimal shifted time and window size are established to enhance these relationships. A summary of all the conditions for each station can be found in Table 2. A median of the best conditions shows the strongest negative correlation at 05:00–07:00 LT, with an 8.5 hr delay and a 17 hr moving average window. Figure 10 illustrates how the relationship between $\Delta NmF2_{perc}$ and GA varies among different ionosonde stations over 5 SCs during local summer in morning hours. Again, the dots on each plot represent the median $\Delta NmF2_{perc}$ value calculated using a moving bin of 2 Kpm during three-hour periods in the local summer months. The optimal shifted time and window size are used for each station accordingly. In the cases of Chilton, Juliusruh, and Moscow, the median value for SC24 appears to be slightly higher than the others for Kpm 5; however, the differences are not statistically significant.

Table 2
Summary of Results for Local Summer and Winter for all Ionosonde Stations Analyzed

	Local summer			Local winter		
Station name	**HCT**[a]	**Delay**[b]	**WS**[c]	**HCT**[a]	**Delay**[b]	**WS**[c]
Boulder	(5–7)	8	17	(17–19)	3	3
Slough/Chilton	(4–6)	9	18	(16–18)	4	4
Juliusruh	(5–7)	9	17	(15–17)	3	3
Moscow	(5–7)	8	15	(16–18)	4	3
Port Stanley	(4–6)	7	12	(17–19)	4	12
Hobart	(6–8)	9	20	(18–20)	3	3
Median Value	(5–7)	8.5	17	(17–19)	3.5	3

[a] HCT are the LT hours corresponding to the highest correlation of $\Delta NmF2_{perc}$ and Kpm. [b] Delay indicates the number of hours by which the correlation is delayed. [c] WS represents the window size in hours used to compute the highest correlation.

Only in Hobart (HO54K), the median values for SC24 are notably higher than those of the other SCs. Nevertheless, no systematic differences can be seen between other SCs.

Figure 11 shows the annual mean of ΔNmF2perc from Juliusruh for years of low solar activity (left panel) and high solar activity (right panel). The points represent the annual averages of ΔNmF2perc for the summer months, separated by Kpm indices of 3, 4, and 5–6. Annual means calculated from fewer than three data points were excluded from the analysis. The lines show the linear fits for each Kpm group, and the legend provides the slope (“sl”) and the corresponding p-value (“p”) for each case.

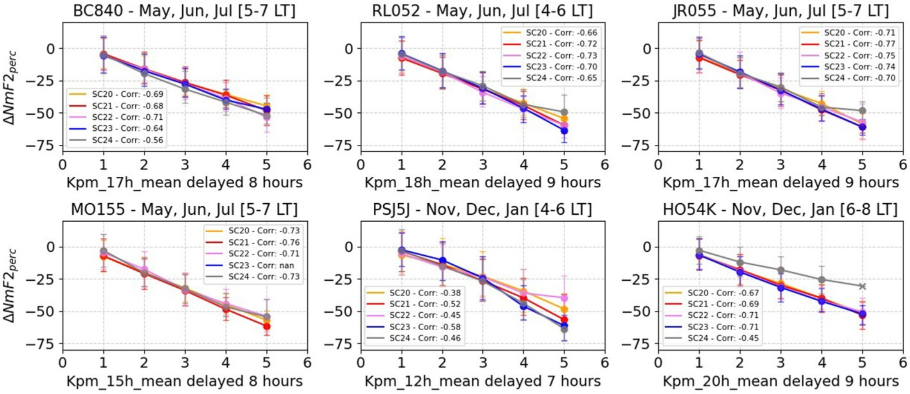

Figure 10. Each plot represents the median values for $\Delta NmF2_{perc}$ data for local summer months between three morning local time hour in a 2 Kpm moving window with steps of 1 Kpm for each solar cycle separately. The error bars represent their corresponding lower and upper quartiles. Analysis includes Northern Hemisphere ionosonde stations (Boulder: BC840; Slough/Chilton: RL052; Juliusruh: JR055; Moscow: MO155) during May, June, and July, and Southern Hemisphere stations (Port Stanley: PSJ5J; Hobart: HO54K) during November, December, and January.

In all cases, the p-values are greater than 0.05, indicating that the slopes are not statistically significant. Therefore, no clear trend in the *NmF*2 response to GA can be confirmed from this analysis. As can be seen, even when using this simple and alternative approach to examine the trend in the *NmF*2 response to GA, the result remains consistent with that shown previously in Figure 10.

3.2. Positive Correlation Between ΔNmF2 and GA During Winter Afternoon

Figure 12 displays the correlation heat map for all six stations during three local winter months: November, December, and January in the Northern Hemisphere, and May, June, and July in the Southern Hemisphere. Purple contour lines enclose regions where the correlation values are not statistically significant, mostly observed next to region of positive correlations.

In general, the pattern in the heat maps is less clear under winter conditions compared to summer. All correlation heat maps exhibit the highest positive correlation values during the afternoon, specifically with delays of 3–4 hr. However, it is evident that at some stations, the positive correlations are quite low and limited to only a few hours of data. An example of this is Hobart (HO54K). Stations situated at lower geomagnetic latitudes, such as Boulder and Port Stanley, display stronger positive correlations throughout the day, including noon, afternoon, and nighttime hours. According to Mendillo (2006), positive correlations, primarily driven by meridional equatorward winds, are particularly prominent in the American longitude sector due to the offset of the geomagnetic dipole.

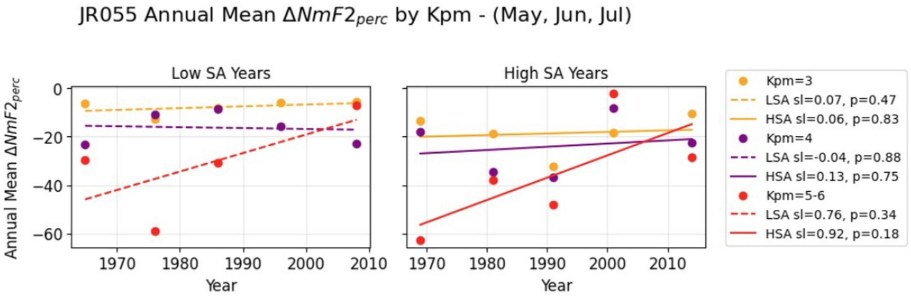

Figure 11. Annual mean of $\Delta NmF2_{perc}$ from Juliusruh for years of low solar activity (left panel) and high solar activity (right panel). Points in yellow correspond to data with Kpm 3, in purple for data with Kpm 4, and in red for data with Kpm 5 and 6. Slashed lines represent the linear fit for each Kpm group in the low solar activity years, while solid lines are used for the high solar activity years.

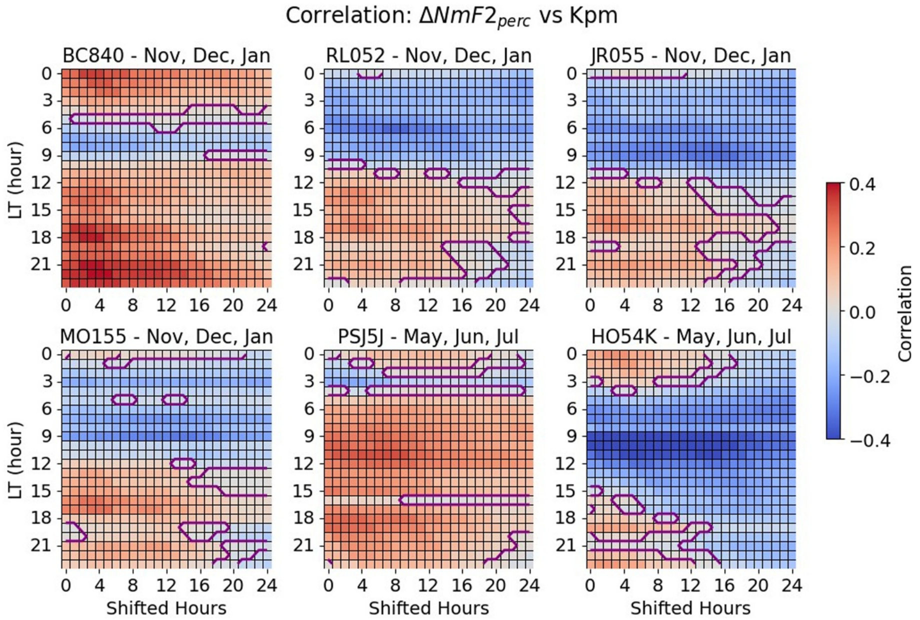

Figure 12. Heat maps showing the maximum absolute correlation values between $\Delta \mathrm{NmF2}_{\mathrm{perc}}$ and Kpm index for each local time hour, including a shifted (delayed) hour during winter months. Analysis includes Northern Hemisphere ionosonde stations (Boulder: BC840; Slough/Chilton: RL052; Juliusruh: JR055; Moscow: MO155) during December, and January and Southern Hemisphere stations (Port Stanley: PSJ5J; Hobart: HO54K) during June, and July. Purple lines encapsulate insignificant correlations.

At all stations, there are two noticeable peaks where the correlation values tend to increase slightly. The first peak typically occurs during the local afternoon hours, while the second peak appears later at night. This pattern is particularly evident in Boulder and Juliusruh. We will focus on the peak around 18 LT.

In the same manner as the summer months, Figures 5 and 6 are recalculated for the winter months at all the ionosonde stations (not shown here). A summary of the conditions that yield the clearest positive response of *NmF*2 to Kpm in winter for each station can be found in Table 2. While these conditions may vary slightly for each station, the median results indicate that the highest positive correlation occurs between 17:00 and 19:00 LT, with a time delay of 3.5 hr and a moving average window of 3 hr. However, it is important to note that Port Stanley is an exception, with a window size of approximately 12 hr, which is significantly different from the median value observed at the other stations.

Like previous analyses, Figure 13 illustrates how the relationship between $\Delta \mathrm{NmF2}_{\mathrm{perc}}$ and GA varies among different ionosonde stations over 5 SCs during afternoon hours in local winter months. In comparison to the summer case shown in Figure 10, larger differences between different SCs is evident at Kpm > 4 at all stations except for MO155. In particular, SC24 shows clear enhancement than previous SCs at BC840, RL052, and JR055 stations. However, no systematic variation can be seen in previous SCs, that is the differences increase or decreases with ascending SCs Furthermore, the correlation values were below 0.3, with some falling below 0.1, demonstrating a generally very weak response to geomagnetic storms in winter at this LT. Thus, these positive responses remain inconclusive.

Table 2 shows median time delays of 8.5 hr for negative storms in summer mornings and 3.5 hr for positive storms in winter afternoons, consistent with J. Liu et al. (2010); W. Liu et al. (2017). Seasonal differences in optimal window size likely reflect physical processes: long summer windows (13–20 hr) capture cumulative energy input from sustained Joule Heating and the resulting DDEF (Richmond & Lu, 2000), while short winter windows (3–4 hr) indicate that rapid GA changes, via PPEF or storm-driven winds, quickly enhance *NmF*2 through vertical plasma uplift, amplified by the higher O/N_2 ratio (Fuller-Rowell et al., 1994; Mendillo, 2006).

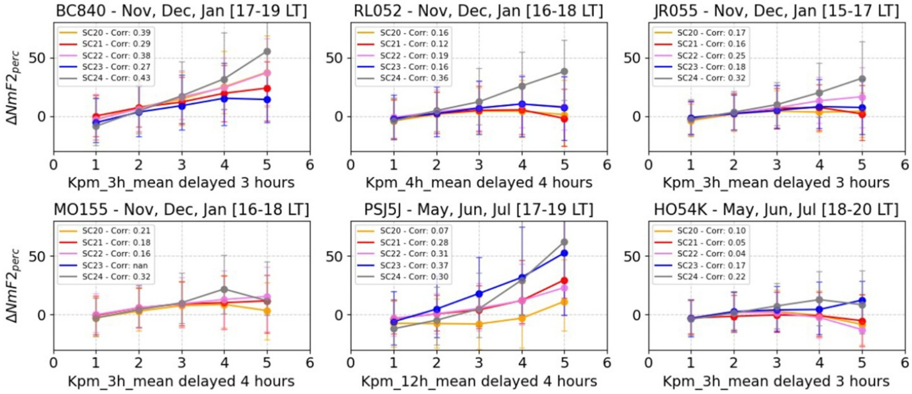

Figure 13. Each plot represents the median values for ΔNmF2$_{\text{perc}}$ data for local winter months between three morning local time hour in a 2 Kpm moving window with steps of 1 Kpm for each solar cycle separately. The error bars represent their corresponding lower and upper quartiles. Analysis includes Northern Hemisphere ionosonde stations (Boulder: BC840; Slough/Chilton: RL052; Juliusruh: JR055; Moscow: MO155) during December, and January and Southern Hemisphere stations (Port Stanley: PSJ5J; Hobart: HO54K) during June, and July.

4. Discussion

In this study, using *NmF*2 data from six ionosonde stations, we focus on how positive and negative ionospheric storm responses vary over time, potentially influenced by increasing atmospheric CO_2 levels. The analysis above indicates that neither response exhibits systematic differences across SCs. This contrasts with the global simulation results of H. Liu et al. (2021) and Pedatella et al. (2025), both of which report distinct differences in the ionospheric response to magnetic storms under low versus high CO_2 conditions. Specifically, H. Liu et al. (2021) shows an enhanced plasma density response when averaged globally, whereas Pedatella et al. (2025) finds that the TEC response varies with latitude, strengthening in auroral and tropical regions but weakening at midlatitudes.

Figures 10 and 13 show no clear long-term trends in the *NmF*2–GA relationship. Possible reasons for the discrepancies between our observational results and the mentioned model results include the following.

1. Difference between global trend and local trend. The model simulations of both H. Liu et al. (2021) and Pedatella et al. (2025) presented global trends averaged over all longitudes, while our results are only from 6 stations in the European, Australian and American sectors. Given the known strong variation of magnetic storm impacts among different sectors, the differences between individual stations (affected by both global and local forcing) and the global simulations are not surprising.
2. Secular variation of the geomagnetic field may complicate the detection of trends. While this variation is not included in the modeling studies of H. Liu et al. (2021) and Pedatella et al. (2025), it is inherently accounted for in our observations. Nevertheless, given the locations of the selected ionosonde stations, long-term geomagnetic changes are expected to be relatively minor, with negligible effects on *NmF*2 (Cnossen & Richmond, 2013).
3. The actual change in CO_2 may be insufficient to produce a measurable effect on the ionosphere, whereas the modeling studies of H. Liu et al. (2021) and Pedatella et al. (2025) used CO_2 values double or triple of the present value.
4. The CO_2 concentration increased from 319 to 409 ppm during the 55 years of observations. In comparison, those in H. Liu et al. (2021) increased from 345 to 690 ppm and those in Pedatella et al. (2025) increased from 400 to 918 ppm. Therefore, the effects predicted in these modeling studies could be difficult to detect in observations, given the much smaller CO_2 increase.
5. Changes in geomagnetic forcing may have occurred over the 55-year analysis period. This possibility is explored in more detail below.

We used Kpm to represent the GA that is driven by solar wind. Is this representation remain the same throughout the SCs? To answer this question, the variation of the Kpm index is analyzed in response to a solar wind parameter known as the Kan-Lee electric field (E_{KL}). This estimated "merging electric field" (Kan & Lee, 1979) reflects the transfer of energy from the solar wind into the magnetosphere. This approach allows us to investigate the variation of GA over time.

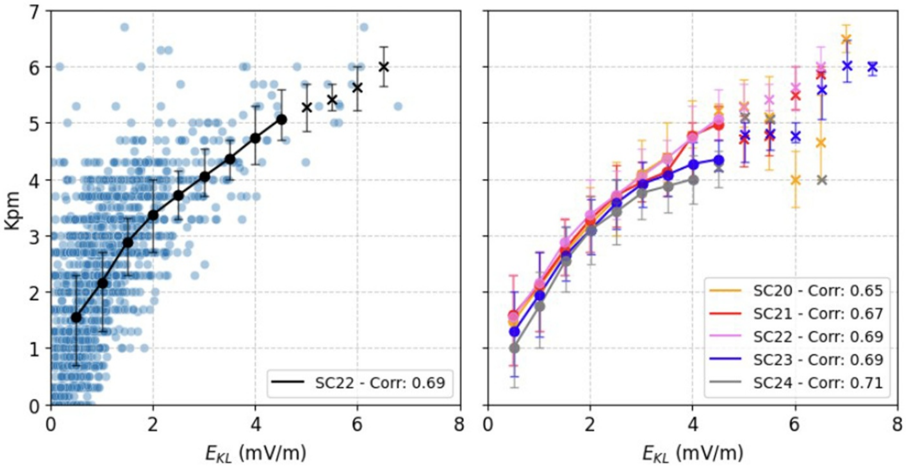

Figure 14. Left panel: Daily median values of Kpm versus E_{KL} in SC22 (blue dots) and median values for each window size of 1 mV/m (E_{KL}) with a step of 0.5 mV/m and their corresponding lower and upper quartiles (black dots with error bars). Right panel: Median values for the daily median values of Kpm in a 1 mV/m moving window with steps of 0.5 mV/m for each solar cycle separately.

The left panel of Figure 14 illustrates the relationship between the Kpm index and E_{KL} for SC22 as an example. The blue dots represent the daily median values. To better demonstrate their response, we utilized a binning-based plotting method, similar to previous analyses. For each SC, the Kpm data have been organized into moving bins size of 1 mV/m (E_{KL}) with a step of 0.5 mV/m. The black dots with error bars indicate the median values of the binned data, positioned at the center of each bin. The error bars correspond to the lower and upper quartiles. Medians based on fewer than 10 values are indicated with crosses to show their limited statistical reliability. The right panel shows the median values of the binned Kpm and E_{KL} for each SC separately. It is seen that Kpm starts to flatten around $\mathrm{Kp} = 4$. Furthermore, for the same Kpm around 4, the E_{KL} tends to be larger during SC24 and SC23 than previous ones, indicating more energy is transferred to the magnetosphere.

Finally, we acknowledge some limitations in our analysis. One key challenge is the limited number of high GA events, which prevents us from drawing robust conclusions for Kpm values greater than 5–6 in all cases. As shown in Figure 2, the scarcity of data during extreme geomagnetic disturbances reduces the statistical reliability of the results for such events. Another limitation, briefly mentioned earlier, is the high variability in the ionospheric response to GA, particularly during winter. The correlation values between $NmF2_{\mathrm{resid}}$ and geomagnetic indices can be extremely low and strongly depend on the station's latitude. As a result, it becomes difficult to perform meaningful long-term comparisons when the parameters of interest do not show consistently significant correlations.

5. Summary and Conclusions

An analysis of hourly data of $NmF2$ derived from six ionospheric stations located at geomagnetic midlatitudes in both hemispheres, covering the last five complete SCs (1964–2019), has been performed. The study examines the $NmF2$ response to GA using four different GA indices (ap, am, Kp, and Kpm). The impact of solar radiation on $NmF2$ is removed before the analysis (using F30 index), and Kpm is selected as the index that generates a higher absolute correlation with the residuals of $NmF2$. The main results of this work are as follows:

- The $NmF2$ response to GA found in this study is consistent with the well-known dominant features of summer and winter storms at midlatitudes. Overall, the response is negative across all months and LT hours, except during local winter months. The strongest correlations are found during local summer months in the morning hours (between 5 and 8 LT). In winter, weak positive correlations appear in the afternoon. This confirms the typical storm behavior, characterized by a dominant negative response in summer mornings and a positive response in winter afternoons.
- Only summer negative storms can be statistically analyzed for trends, as the absolute correlation values are almost always above 0.6. The highest absolute correlations in local summer are obtained with an average time

delay of approximately 8.5 hr, using a moving window of around 17 hr. However, no significant changes in the *NmF*2 response to GA are found over the past 5 SCs, within the Kpm range of 1–5.

- Winter positive storms show very strong variability and low correlation with GA indices, generally below 0.3. The highest positive correlations for local winter months are found around 18 LT, with an average time delay of 3.5 hr and a moving window of 3 hr. The overall low and inconsistent correlation prevents the detection of long-term trends.
- The analysis of the observations did not reveal clear impact of increasing CO_2 on the ionospheric response to GA. This is likely due to insufficient CO_2 rise (in comparison to those used in model predictions), along with the rising solar wind energy in SC 23 and 24. The complex nature of the ionospheric response to solar wind energy input (or GA), which is not yet fully understood, poses a major challenge for detecting such long-term changes.

Conflict of Interest

The authors declare no conflicts of interest relevant to this study.

Data Availability Statement

The F30 data can be accessed from https://spaceweather.cls.fr/services/radioflux/, with daily resolution measurements available since November 1951. The Kp index data used in this study was sourced from the GeoForschungsZentrum located in Potsdam, Germany (https://kp.gfz-potsdam.de/daten).

For Juliusruh *foF2* data, please refer to the World Data Centre web pages at the Australian Space Weather Forecasting Centre (WDC) (https://www.sws.bom.gov.au/World_Data_Centre/1/3).

Boulder data from 1958 to 2002 can be obtained from the UK Solar System Data Centre (UKSSDC), while data from 2002 to 2024 is available from the Digital Ionogram Data Base at the Lowell GIRO (https://giro.uml.edu/didbase/scaled.php).

The Slough/Chilton data from 1931 to 2007 is accessible via UKSSDC (https://www.ukssdc.ac.uk/~matthew.wild@stfc.ac.uk/Slough_foF2_1931–1995.txt, https://www.ukssdc.ac.uk/~matthew.wild@stfc.ac.uk/Chilton_foF2_1993–2007.txt), and from 2007 to 2024, data can be obtained from GIRO.

For Moscow, data from 1957 to 1995 is available through WDC, while data from 2008 to 2022 can be found at GIRO.

Port Stanley data from 1957 to 2007 is accessible from UKSSDC (https://www.ukssdc.ac.uk/~matthew.wild@stfc.ac.uk/Stanley_foF2_1957–2007.txt), with additional data available from 2007 to 2019 from GIRO. Hobart data from 1950 to 2015 can be obtained from WDC, and data from 2015 to 2024 is available from GIRO.

The transformation from geographic to geomagnetic coordinates was performed using https://wdc.kugi.kyoto-u.ac.jp/igrf/gggm/index.html.

Acknowledgments
MGTJR acknowledges support by DLR/DAAD Research Fellowships, Doctoral Studies in Germany (57622551). HL acknowledges support by JSPS grant JP22K21345 and JP25K01058. We thank Norbert Jakowski for generously sharing his expertise and for his valuable comments and suggestions that enhanced this manuscript. Open Access funding enabled and organized by Projekt DEAL.

References

Astafyeva, E., Zakharenkova, I., & Alken, P. (2015). Prompt penetration electric fields and the extreme topside ionospheric response to the June 22–23, 2015, geomagnetic storm as seen by cosmic, swarm, and ground-based instruments. *Journal of Geophysical Research: Space Physics*, *120*(10), 8891–8903. https://doi.org/10.1002/2015JA021328

Bartels, J., Heck, N. H., & Johnston, H. F. (1939). The three-hour-range index measuring geomagnetic activity. *Terrestrial Magnetism and Atmospheric Electricity*, *44*(4), 411–454. https://doi.org/10.1029/te044i004p00411

Blanc, M., & Richmond, A. (1980). The ionospheric disturbance dynamo. *Journal of Geophysical Research*, *85*(A4), 1669–1686. https://doi.org/10.1029/ja085ia04p01669

Blanch, E., Altadill, D., & Torta, J. M. (2012). Behaviour of the ionospheric critical frequencies at European mid-latitudes during high solar activity and large geomagnetic storms. *Advances in Space Research*, *49*(3), 444–456. https://doi.org/10.1016/j.asr.2011.10.012

Bonett, D. G., & Wright, T. A. (2000). Sample size requirements for estimating Pearson, Kendall and Spearman correlations. *Psychometrika*, *65*(1), 23–28. https://doi.org/10.1007/BF02294183

Borries, C., Jakowski, N., Jacobi, C., Hoffmann, P., & Pogoreltsev, A. (2007). Spectral analysis of planetary waves seen in ionospheric total electron content (tec): First results using gps differential tec and stratospheric reanalyses. *Journal of Atmospheric and Solar-Terrestrial Physics*, *69*(17–18), 2442–2451. https://doi.org/10.1016/j.jastp.2007.02.004

Bremer, J. (1998). Trends in the ionospheric e and f regions over europe. *Annales Geophysicae*, *16*(8), 986–996. https://doi.org/10.1007/s00585-998-0986-9

Buonsanto, M. (1999). Ionospheric storms — A review. *Space Science Reviews*, *88*(3/4), 563–601. https://doi.org/10.1023/a:1005107532631

Chakraborty, S., & Morley, S. K. (2020). Probabilistic prediction of geomagnetic storms and the kp index. *Journal of Space Weather and Space Climate*, *10*, 36. https://doi.org/10.1051/swsc/2020037

Chen, Y., Liu, L., Le, H., Zhang, H., & Zhang, R. (2022). Responding trends of ionosphericf2-layer to weaker geomagnetic activities. *Journal of Space Weather and Space Climate*, *12*, 6. https://doi.org/10.1051/swsc/2022005

Cnossen, I., & Franzke, C. (2014). The role of the sun in long-term change in the f2 peak ionosphere: New insights from EEMD and numerical modeling. *Journal of Geophysical Research: Space Physics*, *119*(10), 8610–8623. https://doi.org/10.1002/2014JA020048

Cnossen, I., & Richmond, A. D. (2008). Modelling the effects of changes in the earth's magnetic field from 1957 to 1997 on the ionospheric hmf2 and fof2 parameters. *Journal of Atmospheric and Solar-Terrestrial Physics*, *70*(11–12), 1512–1524. https://doi.org/10.1016/j.jastp.2008.05.003

Cnossen, I., & Richmond, A. D. (2013). Changes in the earth's magnetic field over the past century: Effects on the ionosphere-thermosphere system and solar quiet (sq) magnetic variation. *Journal of Geophysical Research: Space Physics*, *118*(2), 849–858. https://doi.org/10.1029/2012JA018447

Danilov, A. (2013). Ionospheric f-region response to geomagnetic disturbances. *Advances in Space Research*, *52*(3), 343–366. https://doi.org/10.1016/j.asr.2013.04.019

Danilov, A. (2017). New results in studying fo f2 trends. *Journal of Atmospheric and Solar-Terrestrial Physics*, *163*, 103–113. https://doi.org/10.1016/j.jastp.2017.04.002

Danilov, A. D., & Mikhailov, A. V. (1999). Letter to the editor: Spatial and seasonal variations of the fof2 long-term trends. *Annales Geophysicae*, *17*(9), 1239–1243. https://doi.org/10.1007/s00585-999-1239-2

Donaldson, J. K., Wellman, T. J., & Oliver, W. L. (2010). Long-term change in thermospheric temperature above Saint Santin. *Journal of Geophysical Research*, *115*(A11), A11305. https://doi.org/10.1029/2010JA015346

Elias, A. G., de Artigas, M. Z., & de Haro Barbas, B. F. (2010). Trends in the solar quiet geomagnetic field variation linked to the earth's magnetic field secular variation and increasing concentrations of greenhouse gases. *Journal of Geophysical Research*, *115*(A8), A08316. https://doi.org/10.1029/2009JA015136

Fejer, B. G., Blanc, M., & Richmond, A. D. (2016). Post-storm middle and low-latitude ionospheric electric fields effects. *Space Science Reviews*, *206*(1–4), 407–429. https://doi.org/10.1007/s11214-016-0320-x

Field, P., & Rishbeth, H. (1997). The response of the ionospheric f2-layer to geomagnetic activity: An analysis of worldwide data. *Journal of Atmospheric and Solar-Terrestrial Physics*, *59*(2), 163–180. https://doi.org/10.1016/s1364-6826(96)00085-5

Fuller-Rowell, T. J., Codrescu, M. V., Moffett, R. J., & Quegan, S. (1994). Response of the thermosphere and ionosphere to geomagnetic storms. *Journal of Geophysical Research*, *99*(A3), 3893–3914. https://doi.org/10.1029/93JA02015

Fuller-Rowell, T. J., Codrescu, M. V., & Wilkinson, P. (1996). Quantitative modeling of the ionospheric response to geomagnetic activity. *Annales Geophysicae*, *14*, 571–579. https://doi.org/10.1007/s00585-996-0571-0

Jakowski, N., Hoque, M. M., & Mielich, J. (2024). Long-term relationships of ionospheric electron density with solar activity. *Journal of Space Weather and Space Climate*, *14*, 24. https://doi.org/10.1051/swsc/2024023

Kan, J. R., & Lee, L. C. (1979). Energy coupling function and solar wind-magnetosphere dynamo. *Geophysical Research Letters*, *6*(7), 577–580. https://doi.org/10.1029/GL006i007p00577

Laštovička, J. (2024). Dependence of long-term trends in fof2 at middle latitudes on different solar activity proxies. *Advances in Space Research*, *73*(1), 685–689. https://doi.org/10.1016/j.asr.2023.09.047

Lei, J., Wang, W., Burns, A. G., Solomon, S. C., & Richmond, A. D. (2008). Intense storm-time ionospheric response at the low and middle latitudes: A case study of the 2006 December storm. *Journal of Geophysical Research*, *113*(A5), e2020JA028964. https://doi.org/10.1029/2008JA013114

Liu, H., Tao, C., Jin, H., & Abe, T. (2021). Geomagnetic activity effects on co2-driven trend in the thermosphere and ionosphere: Ideal model experiments with gaia. *Journal of Geophysical Research: Space Physics*, *126*(1), e2020JA028607. https://doi.org/10.1029/2020JA028607

Liu, H., Tao, C., Jin, H., & Nakamoto, Y. (2020). Circulation and tides in a cooler upper atmosphere: Dynamical effects of co2 doubling. *Geophysical Research Letters*, *47*(10), e2020GL087413. https://doi.org/10.1029/2020GL087413

Liu, J., Zhao, B., & Liu, L. (2010). Time delay and duration of ionospheric total electron content responses to geomagnetic disturbances. *Annales Geophysicae*, *28*(3), 795–805. https://doi.org/10.5194/angeo-28-795-2010

Liu, W., Xu, L., Xiong, C., & Xu, J. (2017). The ionospheric storms in the American sector and their longitudinal dependence at the northern middle latitudes. *Advances in Space Research*, *59*(2), 603–613. https://doi.org/10.1016/j.asr.2016.10.032

Malhotra, G., Fuller-Rowell, T., Fang, T., Yudin, V., Karol, S., Becker, E., & Kubaryk, A. M. (2025). Medium-scale thermospheric gravity waves in the high-resolution whole atmosphere model: Seasonal, local time, and longitudinal variations. *Journal of Geophysical Research: Atmospheres*, *130*(1), e2024JD041810. https://doi.org/10.1029/2024jd041810

Matzka, J., Stolle, C., Yamazaki, Y., Bronkalla, O., & Morschhauser, A. (2021). The geomagnetic kp index and derived indices of geomagnetic activity. *Space Weather*, *19*(5), e2020SW002641. https://doi.org/10.1029/2020SW002641

Mayaud, P. N. (1980). Derivation, meaning, and use of geomagnetic indices. *American Geophysical Union*. https://doi.org/10.1029/gm022

Mendillo, M. (2006). Storms in the ionosphere: Patterns and processes for total electron content. *Reviews of Geophysics*, *44*(4), RG4001. https://doi.org/10.1029/2005rg000193

Mendillo, M., Lin, C. H., & Huang, C. S. (2002). Variability of ionospheric total electron content: A study of solar-geomagnetic and seasonal effects. *Journal of Atmospheric and Solar-Terrestrial Physics*, *64*(14), 1911–1923. https://doi.org/10.1016/S1364-6826(02)00188-6

Mikhailov, A. V., & Marin, D. (2000). Geomagnetic control of the fof2 long-term trends. *Annales Geophysicae*, *18*(6), 653–665. https://doi.org/10.1007/s00585-000-0653-2

Mikhailov, A. V., Marin, D., Leschinskaya, T. Y., & Herraiz, M. (2002). A revised approach to the fof2 long-term trends analysis. *Annales Geophysicae*, *20*(10), 1663–1675. https://doi.org/10.5194/angeo-20-1663-2002

Pedatella, N. M., Liu, H., Liu, H.-L., Herrington, A., & McInerney, J. (2025). Impact of increasing greenhouse gases on the ionosphere and thermosphere response to a May 2024-like geomagnetic superstorm. *Geophysical Research Letters*, *52*(12), e2025GL116445. https://doi.org/10.1029/2025GL116445

Piggott, W. R., & Rawer, K. (1978). Ursi handbook of ionogram interpretation and reduction November 1972, revision of chapters 1-4. Retrieved from https://ui.adsabs.harvard.edu/abs/1978iirs.rept…P.2nd ed.

Prölss, G. W. (1995). Ionospheric f region storms. In H. Volland (Ed.), *Handbook of atmospheric electrodynamics* (Vol. 2, pp. 195–248). CRC Press.

Prölss, G. W. (2013). Ionospheric storms at mid-latitude: A short review. In *Midlatitude ionospheric dynamics and disturbances* (pp. 9–24). American Geophysical Union. https://doi.org/10.1029/181gm03

Richmond, A., & Lu, G. (2000). Upper-atmospheric effects of magnetic storms: A brief tutorial. *Journal of Atmospheric and Solar-Terrestrial Physics*, *62*(12), 1115–1127. https://doi.org/10.1016/s1364-6826(00)00094-8

Rishbeth, H., Müller-Wodarg, I. C. F., Zou, L., Fuller-Rowell, T. J., Millward, G. H., Moffett, R. J., et al. (2000). Annual and semiannual variations in the ionospheric f2-layer: Ii. Physical discussion. *Annales Geophysicae*, *18*(8), 945–956. https://doi.org/10.1007/s00585-000-0945-6

Roble, R. G., & Dickinson, R. E. (1989). How will changes in carbon dioxide and methane modify the mean structure of the mesosphere and thermosphere? *Geophysical Research Letters*, *16*(12), 1441–1444. https://doi.org/10.1029/GL016i012p01441

Tan Jun Rios, M. G., Borries, C., Liu, H., & Mielich, J. (2025). Long-term changes in the dependence of nmf2 on solar flux at Juliusruh. *Annales Geophysicae*, *43*(1), 73–89. https://doi.org/10.5194/angeo-43-73-2025

Tsurutani, B. T., Verkhoglyadova, O. P., Mannucci, A. J., Lakhina, G. S., Huba, J. D., & Kozyra, J. U. (2004). The interplanetary causes of geomagnetic activity during the October–November 2003 superstorms: A review. *Planetary and Space Science*, *52*(1–3), 139–156. https://doi.org/10.1016/j.pss.2004.09.023

Upadhyay, H. O., & Mahajan, K. K. (1998). Atmospheric greenhouse effect and ionospheric trends. *Geophysical Research Letters*, *25*(17), 3375–3378. https://doi.org/10.1029/98GL02503

Yamazaki, Y., Matzka, J., Stolle, C., Kervalishvili, G., Rauberg, J., Bronkalla, O., et al. (2022). Geomagnetic activity index hpo. *Geophysical Research Letters*, *49*(10), e2022GL098860. https://doi.org/10.1029/2022GL098860

Yue, X., Liu, L., Wan, W., Wei, Y., & Ren, Z. (2008). Modeling the effects of secular variation of geomagnetic field orientation on the ionospheric long term trend over the past century. *Journal of Geophysical Research*, *113*(A10), A10301. https://doi.org/10.1029/2007JA012995

Zhang, S., & Holt, J. M. (2013). Long-term ionospheric cooling: Dependency on local time, season, solar activity, and geomagnetic activity. *Journal of Geophysical Research: Space Physics*, *118*(6), 3719–3730. https://doi.org/10.1002/jgra.50306

Zou, Y., Nishitani, N., Kikuchi, T., Tsugawa, T., & Sato, N. (2014). Local time and seasonal dependence of storm-time midlatitude ionospheric electric fields observed by the superdarn Hokkaido radar. *Journal of Geophysical Research: Space Physics*, *119*(5), 3834–3846. https://doi.org/10.1002/2013JA019692